Hyperpolarized krypton-83 as a contrast agent for magnetic resonance imaging

Galina E. Pavlovskaya*, Zackary I. Cleveland*, Karl F. Stupic*, Randall J. Basaraba†, and Thomas Meersmann*‡

Departments of *Chemistry and †Microbiology, Immunology and Pathology, Colorado State University, Fort Collins, CO 80523

Communicated by Alexander Pines, University of California, Berkeley, CA, October 28, 2005 (received for review June 23, 2005)

For the first time, magnetic resonance imaging (MRI) with hyperpolarized (hp) krypton-83 (^{83}Kr) has become available. The relaxation of the nuclear spin of ^{83}Kr atoms ($I = 9/2$) is driven by quadrupolar interactions during brief adsorption periods on surrounding material interfaces. Experiments in model systems reveal that the longitudinal relaxation of hp ^{83}Kr gas strongly depends on the chemical composition of the materials. The relaxation-weighted contrast in hp ^{83}Kr MRI allows for the distinction between hydrophobic and hydrophilic surfaces. The feasibility of hp ^{83}Kr MRI of airways is tested in canine lung tissue by using krypton gas with natural abundance isotopic distribution. Additionally, the influence of magnetic field strength and the presence of a breathable concentration of molecular oxygen on longitudinal relaxation are investigated.

NMR | optical pumping | pulmonary | MRI | xenon

High nuclear spin polarization in noble gasses can be generated through rubidium vapor spin exchange optical pumping (RbSEOP) (1) and allows for NMR signal enhancements of many orders of magnitude (2). Hyperpolarized (hp) ^{3}He and hp ^{129}Xe (both $I = 1/2$) have both been used in a wide range of NMR and magnetic resonance imaging (MRI) experiments that are otherwise impossible (3–15). In particular hp ^{3}He has been applied for medical MRI diagnosis of pulmonary diseases (16–19). One of the fundamental parameters with high diagnostic value for hp ^{3}He MRI is the spin-density that is a result of the helium concentration in a particular volume. Spin-density mapping of hp ^{3}He can be applied to visualize ventilation in lungs. Other useful parameters are ^{3}He diffusion that provides information about alveolar size distributions in lung tissue and hp ^{3}He relaxation that depends on oxygen partial pressure in lungs. *In vivo* MRI of airways with hp ^{129}Xe as a contrast agent (19–21) suffers from a lower sensitivity compared with hp ^{3}He. However, ^{129}Xe adds a further parameter not available by ^{3}He, namely, the chemical shift that allows for insights into the local environment of the xenon atoms (22–27). The ^{129}Xe chemical shift has been used extensively for research in materials science, engineering, and xenon dissolved in liquids including human blood (3, 5, 6, 8, 9, 12, 28). The chemical shift obtained from hp ^{129}Xe can be used to generate an *in vivo* MRI contrast that is a probe for gas perfusion in lungs (i.e., exchange of the gaseous xenon with the lung parenchyma) (29).

^{3}He and ^{129}Xe are the only spin $I = 1/2$ stable isotopes of the noble gas group, but there are three more NMR active isotopes in this group with higher spin that possess a nuclear electric quadrupole moment. The three quadrupolar isotopes are ^{21}Ne ($I = 3/2$, natural abundance 0.27%), ^{83}Kr ($I = 9/2$, natural abundance 11.5%), and ^{131}Xe ($I = 3/2$, natural abundance 21%). Quadrupolar interactions in these noble gas atoms cause spin relaxation and coherent spin evolution that are probes for the shape, size, and symmetry of void spaces as well as the chemical composition of surfaces in porous media (30–35). Thus, the information provided is highly complementary to that obtained from ^{3}He and ^{129}Xe. Thermally polarized liquid ^{131}Xe was used previously (36) to generate a relaxation-weighted MRI contrast in aerogels that depended on the adsorption of water onto the surface. Unfortunately, low thermal signal intensities make conventional gas-phase MRI of quadrupolar noble gasses impractical. Although ^{83}Kr optical pumping has been explored in the past (37), the wealth of information that is provided by quadrupolar noble gas isotopes can only be used for *in vivo* MRI if optical pumping of quadrupolar gasses followed by a subsequent removal of the alkali metal vapor from the spin exchange process is successful. This goal has recently been achieved for ^{83}Kr with enhancement factors of up to 1,200 times that of the thermal equilibrium signal at 9.4 T (50). This contribution reports the use of the alkali metal-free hp ^{83}Kr for void space imaging in porous materials and *in vitro* biological tissues. Hp ^{83}Kr is introduced as a previously undescribed MRI contrast agent for distinguishing the chemical composition of surfaces in materials imaging with potential applications for medical MRI.

Materials and Methods

NMR and MRI Instrumentation. Experiments were performed on a Chemagnetics CMX II 400 MHz NMR spectrometer in a 9.4 T wide-bore (89 mm) superconducting magnet. The magnet is equipped with an imaging system (Resonance Research, Billerica, MA) consisting of triple axis gradient coils (100 G/cm *x*, *y* axes and 720 G/cm *z* axis) and low-noise linear gradient amplifiers. All NMR spectra and MRI images were obtained by using a custom-built gas flow probe tuned to the ^{83}Kr frequency of 15.4 MHz. All images were acquired with a standard gradient–echo sequence. Continuous-flow images were acquired in 2 h with 32 phase-encoding gradients. Stop-flow images were acquired with 16 phase-encoding gradients with 10- to 15-min polarization time between consecutive acquisitions. A single stopped-flow pumping cycle of 15-min polarization time is used for the FLASH imaging experiment. The subsequent image reconstruction was performed in MATLAB (Version 14.2; Mathworks, Natick, MA).

Optical Pumping and Transfer of Krypton. Production of rubidium-free hp ^{83}Kr through RbSEOP of research-grade krypton (99.995%, natural abundance; Airgas, Radnor, PA) was performed in a cylindrical Pyrex cell (length = 125 mm, i.d. = 24 mm). The gas mixture used in all experiments consists of 95% krypton and 5% molecular nitrogen [N_2 added for radiation-quenching purposes (38)]. The pump cell containing 2.5–5.0 g of rubidium (99.6%; Sigma–Aldrich) was housed in a quartz and aluminum oven to maintain even heating (temperature $\approx$ 433 K). Light (794.7 nm) from the FAP diode-array laser system (line width 2 nm; Coherent, Santa Clara, CA) was directed through a circular polarizer onto the pumping cell. Laser power adjusted to either 30 or 60 W was applied for the pumping process.

In continuous-flow experiments the pressure in the pumping cell was kept above ambient (175 kPa) to avoid contamination by atmospheric oxygen and water vapor. The gas mixture was

Conflict of interest statement: No conflicts declared.

Abbreviations: RbSEOP, rubidium spin exchange optical pumping; hp, hyperpolarized.

‡To whom correspondence should be addressed. E-mail: meer@lamar.colostate.edu or meer@magneticresonance.us.

recirculated by using a peristaltic pump (Watson–Marlow Bredel, Wilmington, MA) (39). The flow rate was monitored with a direct-reading flow meter (Gilmont, Great Neck, NY) and converted for the applied gas mixture. A 27-fold NMR signal enhancement compared with thermally polarized ^{83}Kr at ambient temperature and 9.4-T field strength is obtained.

Alternatively, a batch mode type of experiment is applied. In the batch mode experiments the flow is stopped for 10–15 min, and subsequently the hp krypton is released into a preevacuated detection cell (the sample is evacuated to 0.1 kPa) via PFA tubing. During transfer the gas mixture passes through a water-cooled glass wool filter (≈289 K) to trap rubidium vapor. The technique leads to signal enhancement of ≈1,200 times greater than the thermal signal at 9.4 T and 298 K. The 40-fold improvement of polarization in the batch mode experiment over the continuous-flow experiment is a combinational effect due to the prolonged pumping time and reduced polarization losses during the transfer between the optical pumping cell and the detection cell.

Preparation of Porous Polymer Sample. The 70-μm porous polymer sample (Small Parts, Miami Lakes, FL) was degassed overnight at pressure of <0.1 Pa and stored under dry nitrogen until use.

Preparation and Characterization of Canine Lung Tissue. After humane euthanasia, the lung, heart, and mediastinal connective tissue were removed *en bloc*. The lungs were then separated, rinsed with tap water for 24 h via tracheal infusion, and dried by tracheal insufflations with compressed air for 24 h. The lung tissue samples are cut into cylinders, degassed overnight at <0.1 Pa, and stored under dry nitrogen until use. For the micrograph, desiccated lung tissue was removed and routinely processed for histopathology. Briefly, the sample was rehydrated in 10% neutral buffered formalin, processed through a series of alcohol and xylene solutions, embedded in paraffin, serially sectioned at 4–6 μm, and stained with hematoxylin and eosin for histological examination.

Preparation of Glass Beads. Glass beads with 1.0-mm diameter (Biospec Products, Bartlesville, OK) were degassed overnight at a pressure of <0.1 Pa and stored under dry nitrogen until use. Partially hydrophilic beads were used as obtained from the supplier except for the overnight degassing. Hydrophobic glass beads were prepared by first washing untreated beads for 15 min with a 1:1:5 solution of 30% (vol/vol) NH_4OH, 30% (vol/vol) H_2O_2, and distilled water while stirring vigorously. After NH_4OH/H_2O_2 treatment, the beads were washed for 15 min at 358 K with a 1:1:5 solution of 30% (vol/vol) HCl, 30% (vol/vol) H_2O_2, and distilled water while stirring vigorously. The beads were then washed five times with distilled water and dried in a vacuum desiccator at 523 K for 1 h. The beads were siliconized with 1:10 mixture of SurfaSil (Pierce) in acetone and washed with distilled water in accordance with the manufacturer's instructions.

Calculating T_1 from Optical Pumping Data. T_1 values from optical pumping data are calculated by nonlinear least-squares fitting of the ^{83}Kr signal as a function of time and number of applied medium flip angle (≈12°) rf pulses.

Results and Discussion

Hp–^{83}Kr MRI in the Continuous-Flow Mode. Fig. 1*A* shows a continuous-flow hp ^{83}Kr magnetic resonance image of a phantom using krypton in bulk gas phase between glass structures. The hp ^{83}Kr is generated in continuous flow mode with polarization enhancement factors of <30 (see *Materials and Methods* for details). The obtained resolution is 270 × 270 μm after zero-filling the data size of both dimensions to 64. The overall duration of the MRI experiment is 1.7 h. The continuous-flow type of experiment and the long experimental times are clearly prohibitive for medical applications but may be of use for materials science applications. The batch mode type of experiment will be required for medical MRI, but some of the findings of this section are also relevant for *in vivo* MRI.

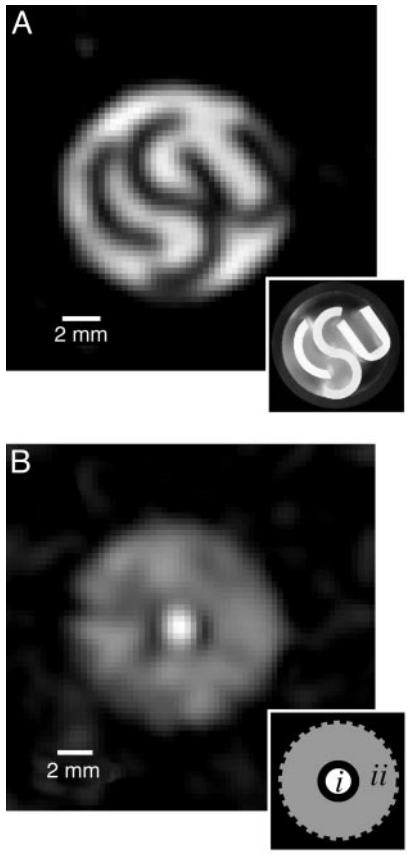

Fig. 1. ^{83}Kr MRI using continuous-flow mode optical pumping. (*A*) Hp ^{83}Kr MRI of gas flowing around glass structures. (*Inset*) A photograph of the phantom used to produce the MRI. Gas flow was held constant at 125 cm^3/min. All figures are displayed after zero-filling. (*B*) Hp ^{83}Kr MRI of a porous polyethylene sample with 70-μm average pore size obtained under continuous flow (100 cm^3/min) conditions. (*Inset*) Sketch of the phantom used for the MRI. The center of the sample (*i*) is a 1.65-mm void space surrounded by a 0.76-mm PFA wall and an 11-mm wide area of a porous polymer (*ii*). The measurement at 9.4 T took ≈2.1 h and led to a resolution of 650 × 650 μm (raw data).

Although the feasibility of void space imaging of bulk gas phase is demonstrated in Fig. 1*A*, porous materials may cause significant problems because of vastly accelerated quadrupolar relaxation in these media. The ^{83}Kr T_1 relaxation time at 175 kPa pressure in 4- to 5-cm-long glass cylinders maintained at 289 K with 11- to 12.4-mm inner diameters are determined to be between 90 and 150 s at 9.4 T (40). These values are substantially shorter than the expected longitudinal relaxation time for ^{83}Kr of T_1 = 470 s, which one would measure in the absence of a container wall at 300 K, 100 kPa, and 2.1 T as reported in ref. 41. The presence of the glass surface greatly accelerates longitudinal relaxation of ^{83}Kr, and the longitudinal relaxation was found to be a function of the surface-to-volume ratio (40). Longitudinal relaxation times between 2.5 and 5.9 s have been measured in various porous polyethylene samples with average pore sizes ranging from 70 to 250 μm and with different chemical surface compositions (hydrophilic and hydrophobic) (40). Fig. 1*B* shows an MRI image taken of a

phantom containing a porous polymer with 70-μm average pore size that demonstrates the feasibility of hp ^{83}Kr MRI in materials with pore dimension well below the alveolar size range. The ^{83}Kr longitudinal relaxation times generally decrease with decreasing pore sizes in materials, and the typical range of human alveolar diameters is 330–480 μm (42).

Relaxation Measurements in Lung Tissue. For *in vivo* MRI studies of airways the ^{83}Kr relaxation times in the lung tissue cannot be significantly shorter than the time scale of the gas transport into the lung. The results from Fig. 1*B* show great promise for biological tissue applications; however, batch mode RbSEOP will have to be applied for any *in vivo* MRI experiments. In addition, longer transport times will be required to accommodate breathing cycles of ≈10 s. To obtain a first estimate of pulmonary T_1 times, a desiccated canine lung tissue sample was prepared (see *Materials and Methods*) that is structurally similar to *in vivo* samples (see Fig. 2*A*). The spin-lattice relaxation time of hp ^{83}Kr at 9.4 T and 289 K is determined to be $T_1 = 10.5$ s. However, molecular oxygen will also be present in the hp ^{83}Kr mixture for *in vivo* MRI applications. Because quadrupolar interactions dominate the relaxation mechanism, the krypton T_1 relaxation time in the canine lung is found to be only partially affected by the presence of 20% oxygen leading to a slightly reduced longitudinal relaxation time of $T_1 = 8.6$ s. This finding is in clear contrast to ^{3}He and ^{129}Xe where the longitudinal relaxation times are entirely regulated by the oxygen partial pressure and can be lowered by orders of magnitude ($T_1 = 10$–20 s) in lungs (19).

Although the ^{83}Kr relaxation times at 9.4 T are long enough for MRI applications, a field dependence of the longitudinal relaxation rates has been observed (50). A remote detection technique was applied to hp ^{83}Kr in a desiccated canine lung sample to assess the potential problem of increased relaxation at field strengths currently used in commercial MRI scanners. The longitudinal relaxation times were found to be field dependent with 5 s at 1.5 T and $T_1 = 7$ s at 3 T, respectively. *In vivo* lung samples may display longer relaxation times under the same conditions, because increasing temperature and water content on the surface has been found to decelerate the ^{83}Kr relaxation rates (Z.I.C., G.E.P., K.F.S., and T.M., unpublished data). Only future *in vivo* studies will provide certainty about the relaxation behavior of ^{83}Kr in lung tissue, but the *in vitro* measurements in this work provide insight into the general trends that are to be expected.

Batch Mode Hp ^{83}Kr MRI of a Desiccated Lung. A desiccated canine lung specimen is selected for the batch mode hp ^{83}Kr MRI proof of concept. Although the chemical composition of the surface will be changed compared with an *in vivo* specimen, the pore structure remains unchanged (Fig. 2*A*). Fig. 2*C* shows an MRI of hp ^{83}Kr MRI in a 10-mm-diameter and 2-cm-long cylindrical sample from a desiccated canine lung specimen using one stopped-flow optical pumping cycle and small flip angle excitation (FLASH). The image was acquired in 46 ms after 15 min of RbSEOP. FLASH experiments are possible because of the enormous enhancement obtained from the stopped-flow experiment and because of the favorable porosity of lung tissue compared with the polymer sample. Note that only ≈31% of the generated spin polarization has been used in this basic FLASH MRI experiment with krypton gas at natural abundance. Fig. 2*B* shows the hp ^{83}Kr MRI of a canine lung specimen obtained using multiple stopped-flow optical pumping cycles. The image is reconstructed from 16 individual stopped-flow experiments that correspond to 16 phase-encoding field gradients. A comparison of Fig. 2 *B* and *C* clearly shows the improved signal-to-noise ratio obtained when a cycle of optical pumping is used for each phase-encoding gradient with a 90° flip angle.

The magnetic resonance images in Fig. 2 are obtained at 9.4 T, a field strength that is higher than the 1.5 T commonly used for medical MRI. The signal intensity will decrease linearly with decreasing magnetic field. This dependence is in contrast to thermally polarized samples in conventional MRI that approximately display an inverse square dependence on the external

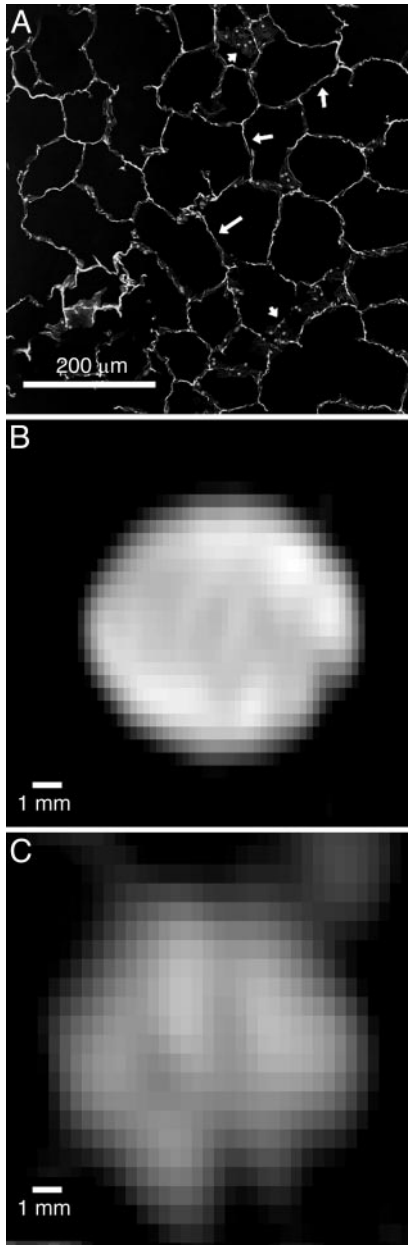

Fig. 2. Hp ^{83}Kr MRI of canine lung tissue using stopped-flow optical pumping. (*A*) Micrograph of lung tissue demonstrating that the drying process preserves the alveolar structure. That microscopic anatomic structure is maintained as evidenced by the intact alveolar septum walls (long arrows) and alveolar epithelium (short arrows). (*B*) ^{83}Kr MRI of canine lung tissue obtained by using krypton stopped-flow optical pumping. The time needed for each of the 16 individual measurements is 10 min for the optical pumping process, ≈3 s for the krypton transfer, and 103 ms for rf pulse, gradient pulse, and acquisition at 9.4-T field strength. The resolution is 480 × 655 μm (raw data) with no slice selection applied. (*C*) ^{83}Kr MRI of a lung sample using only one krypton stopped-flow optical pumping cycle. The measurement takes 15 min for the pumping process, 3 s for the gas transfer, and 0.46 s for the rf pulses, gradient pulses, and signal acquisition. The small flip angle excitation (FLASH) image was produced by using sixteen 12° flip angle pulses. The resolution is 1,080 × 655 μm (raw data) with no slice selection.

magnetic field (43, 44) and is a consequence of the nonequilibrium spin polarization generated by RbSEOP. The maximum spatial resolution is affected by the signal intensity that will be reduced by a factor of ≈6 at 1.5 T compared with the MRI at 9.4 T in Fig. 1. A more significant loss will occur because of the much larger detection coil dimensions in medical MRI. However, improvements beyond a polarization enhancement of ≈3 orders of magnitude are feasible considering a theoretical limit of ≈6 orders of magnitude. Nevertheless, the submillimeter resolution obtained in this work can probably not be maintained for larger samples requiring larger coil diameters. Very clearly, hp ^{83}Kr magnetic resonance will be unable to compete in terms of resolution with hp ^{3}He MRI or even with ^{129}Xe MRI. However, the idea is to introduce a previously undescribed contrast agent for MRI complementary to hp ^{3}He and hp ^{129}Xe as discussed in the following section. Some reduction of spatial resolution may be acceptable as long as it stays within limits that still allow for a meaningful medical diagnosis. The absence of significant anesthetic properties at near atmospheric pressures (45) allows for prolonged times of exposure to hp ^{83}Kr and therefore for more signal averaging. [Note that anesthetic effects are not a problem for any of the other hp noble gas MRI techniques including hp ^{129}Xe because it is commonly used at much lower partial pressures (45, 46)]. A final concern is a trace amount of rubidium that most likely is not completely removed through the relatively simple glass wool filter described in *Materials and Methods*. This problem needs more research and development but is beyond the scope of this work.

Surface-Sensitive Contrast Through Quadrupolar Relaxation. The quadrupolar relaxation experienced by hp ^{83}Kr is a source of contrast that is not available with either hp ^{3}He or hp ^{129}Xe. In the following proof-of-concept demonstration, hp ^{83}Kr is generated by means of stopped-flow optical pumping and used for T_1 relaxation measurements in two samples that are prepared from closest packed 1.0-mm diameter glass spheres. One sample is made of untreated glass beads (i.e., a hydrophilic glass surface), whereas the glass beads in second sample have been treated with the siliconizing agent SurfaSil. In the latter sample, the bead surface has become hydrophobic because of the surface coating with a molecular layer of siloxane. The two systems have been chosen for their simplicity and because void space dimensions, pore symmetry, pore shape, pore connectivity, and porosity remain constant while only the chemical composition of the surface is altered. Furthermore, the void spaces in 1.0-mm closest packed beads have sizes that are similar to alveoli in human lungs (i.e., the octahedral and tetrahedral holes can accommodate spheres with radii up to 414 and 223 μm, respectively). In the untreated hydrophilic sample a ^{83}Kr $T_1 = 35$ s relaxation time is measured, while coating the glass spheres (hydrophobic sample) accelerates the relaxation time to $T_1 = 9$ s. Siliconizing agents have been used for optical pumping experiments in the past (47, 48), because the surface coating insulates the noble gas atoms from magnetic sites in the glass surface (49) and therefore prolongs the lifetime of the hp magnetization in ^{129}Xe and ^{3}He. The previously unknown effect of the coating on ^{83}Kr relaxation is more dramatic, on a completely different time scale, and most importantly, it is reversed! (The optical pumping glassware in hp krypton experiments should therefore not be siliconized.) This effect is caused by the quadrupolar relaxation that becomes more pronounced when the krypton atoms interact with the surface than when they are in the bulk gas phase. The hydrophobic coating causes stronger interactions between the nonpolar noble gas atoms and the surface and hence faster relaxation, whereas the hydrophilic surface causes weaker interactions and results in slower relaxation. Surface-sensitive hp ^{83}Kr MRIs are shown in Fig. 3 *B* and *C*. It is taken from a sample (Fig. 3*A*) that contains the hydrophobic glass beads in the center (*i*) and the hydrophilic glass beads in the outer region (*ii*). The sample has been evacuated before the experiment, and the MRI in Fig. 3*B* was taken ≈3 s after the hp krypton is transferred to the sample to allow the gas pressure to equilibrate. The image shows a weak contrast because the krypton in the sample center

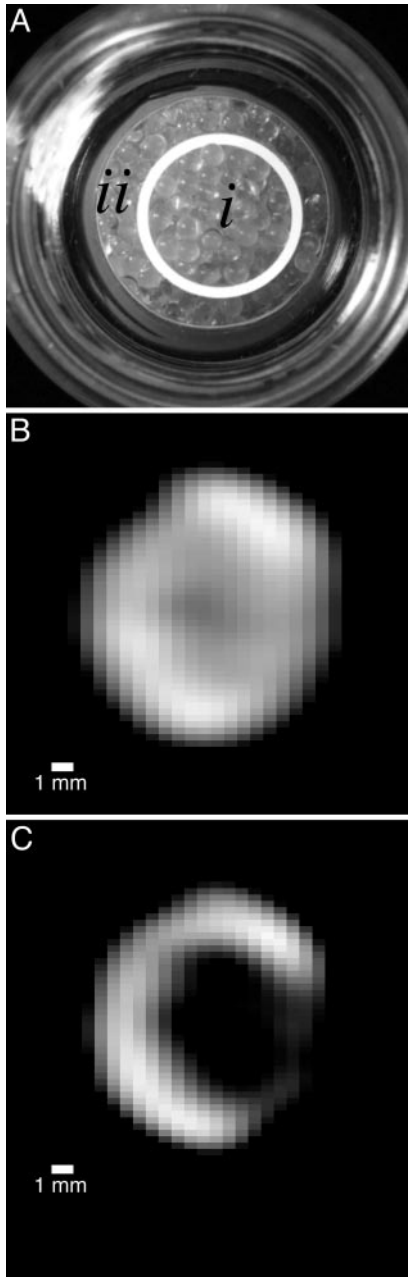

Fig. 3. Hp ^{83}Kr MRI showing surface-sensitive contrast. (*A*) Photograph of the phantom used to obtain surface-dependent contrast. Surface-siliconized 1.0-mm closest packed glass beads (hydrophobic) are located in the center ring (*i*). Separated by an untreated glass tube (seen as a white ring in the photograph because of illumination from below) is the outer region (*ii*) that contains untreated 1.0-mm glass beads (hydrophilic). (*B*) ^{83}Kr MRI of the glass bead sample (*A*) reconstructed from 16 individual krypton stopped-flow optical pumping cycles. The MRI sequence is applied ≈3 s after filling the sample with hp krypton leading to no appreciable MRI contrast between the two regions (note the glass wall is not resolved because the resolution is 424 × 864 μm). (*C*) Same as in *B* except a 9-s waiting period has been added. A clear contrast between the hydrophobic inner sample region ($T_1 = 9$ s) and the hydrophilic outer region ($T_1 = 35$ s) appears. Increasing the waiting time will lead to increased contrast but an overall reduced signal intensity.

is slightly more relaxed than in the outer parts of the sample. The MRI in Fig. 3*C* is recorded under identical conditions except that a delay period of 9 s between gas transfer and signal recording is added. The contrast becomes clearly visible now and demonstrates how hp ^{83}Kr MRI can be used to obtain information about the surface chemistry in porous media.

Conclusions

We have demonstrated the previously undescribed use of a hp noble gas with spin $I > 1/2$ separated from the rubidium vapor of the optical pumping process for MRI in a variety of media. Hp ^{83}Kr magnetic resonance images have been obtained at submillimeter resolution at 9.4 T in porous media with pore sizes similar to alveolar dimensions and in desiccated canine lung tissue at ambient pressure. The ^{83}Kr spin-lattice relaxation times in the lung tissue remain reasonably long and should allow for *in vivo* MRI even in the presence of 20% oxygen. It is shown that hp ^{83}Kr provides a source of contrast that can distinguish between different chemical compositions of surfaces in a simple test system. These results are of potential value for the development of novel *in vivo* MRI techniques that can be used for the diagnosis of lung diseases where the surfactant concentration on the parenchyma surface is affected. Beyond *in vivo* applications, hp ^{83}Kr NMR and MRI will be of importance in materials science for the study of porous media and surfaces. A potential application is the investigation of the homogeneity of surface grafting, coating, and the spatial fluctuations of surface-to-volume ratios in porous media.

Final points are that natural abundance krypton gas (11.5% ^{83}Kr) is affordable (approximately $5 per liter at standard temperature and pressure) and like xenon, but unlike ^{3}He, it can be obtained in a renewable manner from the atmosphere.

We thank S. L. Kraft, D. W. Grainger, and S. B. Hall for stimulating discussions and R. E. Lee and M. D. Olsen for sample preparation. Photographs are by J. A. Mendoza. This material is based on work supported by National Science Foundation Grant CHE-0135082. We thank the donors of the American Chemical Society Petroleum Research Fund under Grant 40625-AC9 for support of the development of ^{83}Kr RbSEOP.

1. Walker, T. G. & Happer, W. (1997) *Rev. Mod. Phys.* **69,** 629–642.
2. Raftery, D., Long, H., Meersmann, T., Grandinetti, P. J., Reven, L. & Pines, A. (1991) *Phys. Rev. Lett.* **66,** 584–587.
3. Goodson, B. M. (2002) *J. Magn. Reson.* **155,** 157–216.
4. Navon, G., Song, Y. Q., Room, T., Appelt, S., Taylor, R. E. & Pines, A. (1996) *Science* **271,** 1848–1851.
5. Raftery, D., MacNamara, E., Fisher, G., Rice, C. V. & Smith, J. (1997) *J. Am. Chem. Soc.* **119,** 8746–8747.
6. Haake, M., Pines, A., Reimer, J. A. & Seydoux, R. (1997) *J. Am. Chem. Soc.* **119,** 11711–11712.
7. Tseng, C. H., Wong, G. P., Pomeroy, V. R., Mair, R. W., Hinton, D. P., Hoffmann, D., Stoner, R. E., Hersman, F. W., Cory, D. G. & Walsworth, R. L. (1998) *Phys. Rev. Lett.* **81,** 3785–3788.
8. Mair, R. W., Wong, G. P., Hoffmann, D., Hurlimann, M. D., Patz, S., Schwartz, L. M. & Walsworth, R. L. (1999) *Phys. Rev. Lett.* **83,** 3324–3327.
9. Anala, S., Pavlovskaya, G. E., Pichumani, P., Dieken, T. J., Olsen, M. D. & Meersmann, T. (2003) *J. Am. Chem. Soc.* **125,** 13298–13302.
10. Moule, A. J., Spence, M. M., Han, S. I., Seeley, J. A., Pierce, K. L., Saxena, S. & Pines, A. (2003) *Proc. Natl. Acad. Sci. USA* **100,** 9122–9127.
11. Dubois, L., Da Silva, P., Landon, C., Huber, J. G., Ponchet, M., Vovelle, F., Berthault, P. & Desvaux, H. (2004) *J. Am. Chem. Soc.* **126,** 15738–15746.
12. Moudrakovski, I. L., Wang, L. Q., Baumann, T., Satcher, J. H., Exarhos, G. J., Ratcliffe, C. I. & Ripmeester, J. A. (2004) *J. Am. Chem. Soc.* **126,** 5052–5053.
13. Jansch, H. J., Gerhard, P. & Koch, M. (2004) *Proc. Natl. Acad. Sci. USA* **101,** 13715–13719.
14. Lowery, T. J., Doucleff, M., Ruiz, E. J., Rubin, S. M., Pines, A. & Wemmer, D. E. (2005) *Protein Sci.* **14,** 848–855.
15. Appelt, S., Hasing, F. W., Kuhn, H., Perlo, J. & Blumich, B. (2005) *Phys. Rev. Lett.* **94,** 197602.
16. MacFall, J. R., Charles, H. C., Black, R. D., Middleton, H., Swartz, J. C., Saam, B., Driehuys, B., Erickson, C., Happer, W., Cates, G. D., *et al.* (1996) *Radiology* **200,** 553–558.
17. Kauczor, H. U., Hofmann, D., Kreitner, K. F., Nilgens, H., Surkau, R., Heil, W., Potthast, A., Knopp, M. V., Otten, E. W. & Thelen, M. (1996) *Radiology* **201,** 564–568.
18. Leawoods, J. C., Yablonskiy, D. A., Saam, B., Gierada, D. S. & Conradi, M. S. (2001) *Concepts Magn. Reson.* **13,** 277–293.
19. Moller, H. E., Chen, X. J., Saam, B., Hagspiel, K. D., Johnson, G. A., Altes, T. A., de Lange, E. E. & Kauczor, H. U. (2002) *Magn. Reson. Med.* **47,** 1029–1051.
20. Albert, M. S., Cates, G. D., Driehuys, B., Happer, W., Saam, B., Springer, C. S. & Wishnia, A. (1994) *Nature* **370,** 199–201.
21. Mugler, J. P., Driehuys, B., Brookeman, J. R., Cates, G. D., Berr, S. S., Bryant, R. G., Daniel, T. M., deLange, E. E., Downs, J. H., Erickson, C. J., *et al.* (1997) *Magn. Reson. Med.* **37,** 809–815.
22. Dybowski, C., Bansal, N. & Duncan, T. M. (1991) *Annu. Rev. Phys. Chem.* **42,** 433–464.
23. Barrie, P. J. & Klinowski, J. (1992) *Prog. NMR Spectrosc.* **24,** 91–108.
24. Raftery, D. & Chmelka, B. F. (1994) *NMR Basic Princ. Prog.* **30,** 111–158.
25. Springuel-Huet, M. A., Bonardet, J. L., Gedeon, A. & Fraissard, J. (1999) *Magn. Reson. Chem.* **37,** S1–S13.
26. Ratcliffe, C. I. (1998) *Annu. Rep. NMR Spectrosc.* **36,** 123–221.
27. Jameson, C. J. (2004) *J. Am. Chem. Soc.* **126,** 10450–10456.
28. Nossov, A., Haddad, E., Guenneau, F. & Gedeon, A. (2003) *Phys. Chem. Chem. Phys.* **5,** 4473–4478.
29. Ruppert, K., Mata, J. F., Brookeman, J. R., Hagspiel, K. D. & Mugler, J. P. (2004) *Magn. Reson. Med.* **51,** 676–687.
30. Jokisaari, J., Ingman, P., Lounila, J., Pulkkinen, O., Diehl, P. & Muenster, O. (1993) *Mol. Phys.* **78,** 41–54.
31. Meersmann, T., Smith, S. A. & Bodenhausen, G. (1998) *Phys. Rev. Lett.* **80,** 1398–1401.
32. Meersmann, T., Deschamps, M. & Bodenhausen, G. (2001) *J. Am. Chem. Soc.* **123,** 941–945.
33. Moudrakovski, I. L., Ratcliffe, C. I. & Ripmeester, J. A. (2001) *J. Am. Chem. Soc.* **123,** 2066–2067.
34. Millot, Y., Man, P. P., Springuel-Huet, M. A. & Fraissard, J. (2001) *Comptes Rendus Acad. Sci. Ser. II Fascicule C Chimie* **4,** 815–818.
35. Horton-Garcia, C. F., Pavlovskaya, G. E. & Meersmann, T. (2005) *J. Am. Chem. Soc.* **127,** 1958–1962.
36. Pavlovskaya, G., Blue, A. K., Gibbs, S. J., Haake, M., Cros, F., Malier, L. & Meersmann, T. (1999) *J. Magn. Reson.* **137,** 258–264.
37. Schaefer, S. R., Cates, G. D. & Happer, W. (1990) *Phys. Rev. A* **41,** 6063–6070.
38. Mortuza, M. G., Anala, S., Pavlovskaya, G. E., Dieken, T. J. & Meersmann, T. (2003) *J. Chem. Phys.* **118,** 1581–1584.
39. Knagge, K., Prange, J. & Raftery, D. (2004) *Chem. Phys. Lett.* **397,** 11–16.
40. Stupic, K. F., Cleveland, Z. I., Pavlovskaya, G. E. & Meersmann, T. (2005) *Solid. State. Nucl. Magn.*, in press.
41. Brinkmann, D. & Kuhn, D. (1980) *Phys. Rev. A* **21,** 163–167.
42. Ochs, M., Nyengaard, L. R., Lung, A., Knudsen, L., Voigt, M., Wahlers, T., Richter, J. & Gundersen, H. J. G. (2004) *Am. J. Respir. Crit. Care* **169,** 120–124.
43. Chen, C. N., Sank, V. J., Cohen, S. M. & Hoult, D. I. (1986) *Magn. Reson. Med.* **3,** 722–729.
44. Hoult, D. I., Chen, C. N. & Sank, V. J. (1986) *Magn. Reson. Med.* **3,** 730–746.
45. Cullen, S. C. & Gross, E. G. (1951) *Science* **113,** 580–582.
46. Ramirez, M. P., Sigaloff, K. C. E., Kubatina, L. V., Donahue, M. A., Venkatesh, A. K. & Albert, M. S. (2000) *NMR Biomed.* **13,** 253–264.
47. Driehuys, B., Cates, G. D. & Happer, W. (1995) *Phys. Rev. Lett.* **74,** 4943–4946.
48. Breeze, S. R., Lang, S., Moudrakovski, I., Ratcliffe, C. I., Ripmeester, J. A., Santyr, G., Simard, B. & Zuger, I. (2000) *J. Appl. Phys.* **87,** 8013–8017.
49. Jacob, R. E., Driehuys, B. & Saam, B. (2003) *Chem. Phys. Lett.* **370,** 261–267.
50. Cleveland, Z. I., Pavlovskaya, G. E., Stupic, K. F., LeNoir, C. F. & Meersmann, T., *J. Chem. Phys.*, in press.